



Parameter optimization of the high-power laser powder bed fusion process for H13 tool steel

Makiko Yonehara¹ · Toshi-Taka Ikeshoji¹ · Takaya Nagahama² · Takashi Mizoguchi² · Makoto Tano² · Takayuki Yoshimi² · Hideki Kyogoku¹

Received: 26 May 2020 / Accepted: 5 August 2020 / Published online: 13 August 2020
© Springer-Verlag London Ltd., part of Springer Nature 2020

Abstract

In this study, process parameter optimization was performed for the powder bed fusion of H13 tool steel under low- (400 W) and high-power (1000 W) conditions using the SLM 280HL machine. The effects of process parameters such as the laser power, scan speed, and hatching pitch on the density and microstructure of the as-built H13 tool steel were investigated. The specimen density was found to be slightly lower under the high-power condition than that under the low-power condition. Electron backscattering diffraction analysis identified that the as-built specimens showed a prolonged columnar microstructure in the build direction under the low-power condition. In contrast, for the specimens fabricated using the hull-core method under the high-power condition, the hull and core parts showed prolonged columnar and equiaxed microstructures, respectively. Phase distribution images indicated that the microstructures of the as-built specimens under the low- and high-power conditions contained martensite (bcc) and austenite (fcc) with a grain size of approximately 1 μm . Thus, it was found that the specimen density achieved using the 400-W laser is higher than that achieved using the 1000-W laser; moreover, the microstructure of the as-built specimen using the 400-W laser is different from that using the 1000-W laser.

Keywords Additive manufacturing · Laser powder bed fusion · Tool steel alloy · Energy density · Density · Microstructure

1 Introduction

Additive manufacturing is an important process for producing products with complex geometries that are difficult to fabricate via conventional processes. In particular, powder bed fusion (PBF) can improve product functionality by realizing three-dimensional complex structures such as lattices and conformal cooling channels. One way of increasing the applicability of this technology in various industrial fields is by expanding the types of materials that can be used in additive manufacturing [1, 2]. With regard to metallic materials, various alloys such as stainless steel, titanium alloy, nickel-based alloy, and aluminum alloy have been employed to produce

parts [1]. With regard to tool steels, previous studies have focused on M2 tool steel [3–5] and H13 tool steel [6] using machines with CO₂ lasers. However, improving the performance of parts in terms of density and surface roughness is difficult via this approach. Thus, machines using Yb-fiber lasers have recently been utilized. Cracks and delamination are known to occur in tool steel because of the high residual stress caused by severe distortion of the martensitic structure due to high carbon content [7]. Therefore, the laser beam powder bed fusion (PBF-LB) process has been used to preheat the baseplate for M2 tool steel [7, 8] and H13 tool steel [9, 10]. The PBF-LB process has been applied to the design of H13 tool steel with conformal cooling channels and lattice structures through injection molding [9, 10].

Several studies have explored the effects of PBF process parameters on the characteristics of the alloy [11–14]. The effects of the fabrication and heat treatment conditions on the microstructure and mechanical properties of AISI H13 hot-work tool steel fabricated via the PBF-LB process have been investigated systematically [15]. Laakso et al. [16] investigated process parameters such as the laser power, scan speed, and hatching pitch for a PBF-LB machine equipped

✉ Hideki Kyogoku
kyogoku@hiro.kindai.ac.jp

¹ Fundamental Technology for Next Generation Research Institute, Kindai University, 1 Takaya-Umenobe, Higashi-Hiroshima, Hiroshima 739-2116, Japan

² Process Technology R&D Department, JTEKT Co., 1-1 Asahi-machi, Kariya, Aichi 448-8652, Japan

with a 400-W single-mode fiber laser and determined the process window for fabricating high-density parts. Holzweissig et al. [17] identified the relationship between the process parameters of PBF-LB and the microstructure of H13 tool steel. Mertens et al. [18] investigated the effect of preheating up to 400 °C on the microstructure and mechanical properties of H13 tool steel. They reported that preheating results in a more homogeneous microstructure with better mechanical properties that are comparable with or even better than those of conventionally fabricated and heat-treated H13 tool steel. Krell et al. [19] investigated the effect of process parameters including the preheating temperature up to 300 °C on the oxygen content and microstructure of H13 tool steel and obtained a relative density of above 99.5%. Wang et al. [20] reported on the high-temperature properties and microstructural stability of H13 tool steel fabricated by the PBF-LB process; they elucidated that the microstructure of the as-built specimen consisted of α -Fe and γ -Fe and that the carbide-stabilizing elements aggregated in cell-like structures for rapid solidification. In addition, the as-built specimens exhibited better mechanical properties than the wrought materials at a test temperature of 600 °C. Narvan et al. [15] investigated the effects of process parameters such as the laser power, scan speed, hatching pitch, and volumetric energy density (or energy density) on the quality of H13 tool steel. They achieved a maximum relative density of 99.7% at an energy density of above 60 J/mm³. They also investigated the surface roughness, microstructure, and hardness of the as-built specimen and found that the microstructure consisted of a fine equiaxed cellular-dendritic structure with martensite and the retained austenite. Thus, these studies were conducted using a low-power (400 W) laser.

As noted earlier, tool steel tends to crack because of residual stress. Yan et al. [21] used transmission electron microscopy (TEM) to examine the microstructure of as-built H13 tool steel and elucidated the mechanism behind the occurrence of residual stress. They found that the PBF-LB process results in the formation of martensite and its partial decomposition into fine α -Fe and Fe₃C precipitates along with retained austenite. The residual stress was in the range of 940–1420 MPa and was mainly attributed to martensitic transformation during processing. Yan et al. [21], Casati et al. [22], and Prudente et al. [23] reported the effect of heat treatment on the microstructure and mechanical properties of as-built H13 tool steel.

Besides processing H13 tool steel, Sander et al. [24] used a PBF-LB machine with preheating equipment allowing temperatures up to 500 °C to successfully process high-strength Fe85Cr4Mo8V2C1 tool steel. They performed parameter optimization to obtain crack-free and highly dense alloy parts (relative density of 99.99%). The as-built alloy showed a microhardness of 900 HV0.1 (ca. 67HRC) and compressive strength of approximately 3800 MPa. Boes et al. [25] investigated the effects of the process parameters and preheating

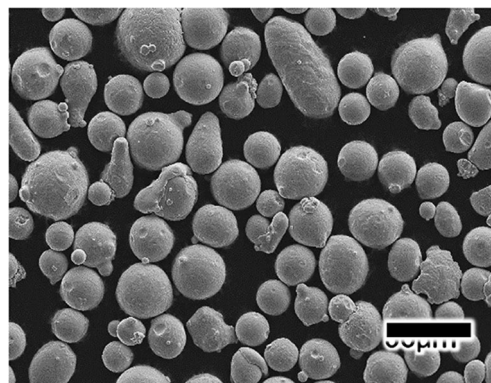


Fig. 1 SEM image of H13 powder

temperature on the microstructure and mechanical properties of X65MoCrWV3-2 cold work tool steel. They obtained a high-density alloy (porosity of less than 0.5 vol%) and found that the microstructure comprised martensite and retained austenite up to a temperature of 500 °C.

The demand for speeding up the PBF-LB process has led to the utilization of multiple lasers, high laser power, and high scan speeds. In previous studies, however, the process was conducted under a laser power of 300 W, in which case the scan speed was limited to ensure an adequate energy density. In this study, parameter optimization was performed on the PBF-LB process for H13 tool steel under low- and high-power conditions using a machine equipped with a 400-W single-mode fiber laser and 1000-W multi-mode fiber laser, and the possibility of speeding up the process using the high-power laser was explored. Moreover, the effects of process parameters such as the laser power, scan speed, and hatching pitch on the density and microstructure of the as-built H13 tool steel were investigated.

2 Experimental procedures

2.1 Powder characteristics

Gas-atomized H13 tool steel powder (LPW H13) was employed for this study. Figure 1 shows a scanning electron

Table 2 Specifications of SLM 280HL machine

Laser	1 × 400-W single-mode fiber laser, 1 × 1000-W multi-mode fiber laser
Laser spot diameter	400 W: 0.08 mm, 1000 W: 0.3 mm
Build size	280 × 280 × 350 mm
Scan speed	Max: 15 m/s
Layer thickness	0.02–0.15 mm

Table 1 Chemical composition of H13 powder (mass%)

	C	Mn	Si	Cr	Ni	Mo	V	Cu	P	S	N	O	Fe
Standard	0.32–0.45	0.20–0.50	0.80–1.20	4.75–5.50	< 0.3	1.10–1.75	0.80–1.20	< 0.25	< 0.03	< 0.03	-	-	Bal.
Powder	0.41	0.44	0.96	5.26	< 0.1	1.53	1.10	< 0.01	< 0.015	0.004	0.04	0.02	Bal.

microscopy (SEM) image of the H13 tool steel, and Table 1 presents the chemical composition. The particle size distribution ranged from 10 to 45 μm , and the D10, D50, and D90 values were 19, 28, and 42 μm , respectively. The flowability of the powder measured using a Hall flowmeter was 2.68 s/50 g, which indicates good flowability.

2.2 Fabrication conditions

A PBF-LB machine (SLM Solutions GmbH, SLM280HL) equipped with a 400-W single-mode fiber laser and 1000-W multi-mode fiber laser, as well as a preheating system for the baseplate to attain a temperature of up to 200 $^{\circ}\text{C}$, was employed. The machine specifications are presented in Table 2. The effects of the following process parameters on the density and microstructure of as-built H13 tool steel were investigated using the 400- and 1000-W lasers: the laser power, scan speed, hatching pitch, and layer thickness. These parameters are shown in Fig. 2. The energy density or volumetric energy density E (J/mm^3) is expressed as

$$E = P/vht, \quad (1)$$

where P is the laser power (W), v is the scan speed (mm/s), h is the hatching pitch (mm), and t is the layer thickness (mm).

Using the 400-W laser, the ranges for the laser power, scan speed, and hatching pitch values were 175–375 W, 400–1000 mm/s, and 0.1–0.14 mm, respectively, and the layer thickness was fixed at 0.05 mm. The range for the energy density was 54.2–114.6 J/mm^3 . Using the 1000-W laser, laser power and scan speeds in the ranges of 600–1000 W and 100–260 mm/s were employed, respectively, and the hatching pitch and layer thickness were fixed at 0.7 and 0.1 mm, respectively. The range for the energy density was 43.4–142.9 J/mm^3 . These fabrication conditions are summarized in Table 3. Experiments were performed in an atmosphere of nitrogen gas with an oxygen content of less than 0.1%, and the baseplate was preheated to a temperature of 200 $^{\circ}\text{C}$.

2.3 Evaluation of characteristics of the specimens

The density of the as-built specimens was measured using the Archimedes method. The relative density was calculated according to the reference density of 7.78 g/cm^3 . The microstructures of the as-built specimens were observed with an optical microscope (OM) after nital etching. The surface

morphology and microscopic microstructure of the specimens were observed via a scanning electron microscope (JEOL JSM-7800F) equipped with electron backscatter diffraction (EBSD).

3 Results and discussion

3.1 Investigation of process parameters

To investigate the influence of the process parameters on the density and microstructure, cuboid specimens with dimensions of 15 mm \times 15 mm \times 30 mm were fabricated using the 400-W laser. However, fabricating cubic specimens using the 1000-W laser was difficult because the high power roughened the specimen surface. Thus, cubic specimens were fabricated using the hull-core method; here, the hull (i.e., outer section) was fabricated using the 400-W laser, and the core (i.e., inner section) was fabricated using the 1000-W fiber laser. The fabricated cubic specimens and the hull-core method are presented in Fig. 3. The thickness of the hull was set to 2 mm, as shown in Fig. 3(b).

3.1.1 Influence of process parameters on density of alloy with 400-W laser

The effects of the process parameters on the density of the as-built specimens were investigated. Figure 4 shows that the relative density increased with the energy density. The relative density was low at 98.5% for an energy density of 60 J/mm^3 , increased to more than 99% at an energy density of more than

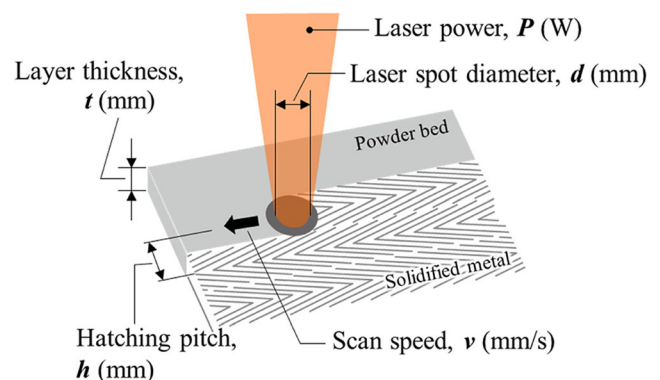


Fig. 2 Schematic of SLM process and various parameters

Table 3 Fabrication conditions

Laser	Parameter	Condition
400 W	Power (P)	175–375 W
	Scan speed (v)	400–1000 mm/s
	Hatching pitch (h)	0.10–0.14 mm
	Layer thickness (t)	0.05 mm
	Energy density (E)	54.2–114.6 J/mm ³
1000 W	Power (P)	600–1000 W
	Scan speed (v)	100–260 mm/s
	Hatching pitch (h)	0.7 mm
	Layer thickness (t)	0.1 mm
	Energy density (E)	43.4–142.9 J/mm ³

65 J/mm³, and became saturated at 99.5% when the energy density was over 80 J/mm³.

To improve the density of the as-built specimens, process parameters such as the laser power, scan speed, and hatching pitch were varied while the energy density of 80 J/mm³ was maintained, and the results were compared with those obtained at an energy density of 57 J/mm³. Figure 5 presents the influence of the scan speed on the relative density of the as-built specimens fabricated using the 400-W laser. Figure 5(a) shows the results with the energy densities of 57 and 80 J/mm³. The relative density of the as-built specimens was higher at an energy density of 80 J/mm³ than at 57 J/mm³, and the maximum relative density was over 99.5% at a scan speed of more than 400 mm/s. Figure 5(b) shows the results with varying laser power. The relative density increased with the laser power and decreased with increasing scan speed when the laser power was fixed. These results, indicated by open circles, correspond to those obtained at an energy density of 57 J/mm³ that are presented in Fig. 5(a). Consequently, the relative density of the as-built specimens was maximized at 99.9% with a laser power of 375 W, scan speed of 790 mm/s, hatching pitch of 0.12 mm, and energy density of 79.1 J/mm³. Åsberg et al. [26] reported that hot isostatic pressing (HIP)

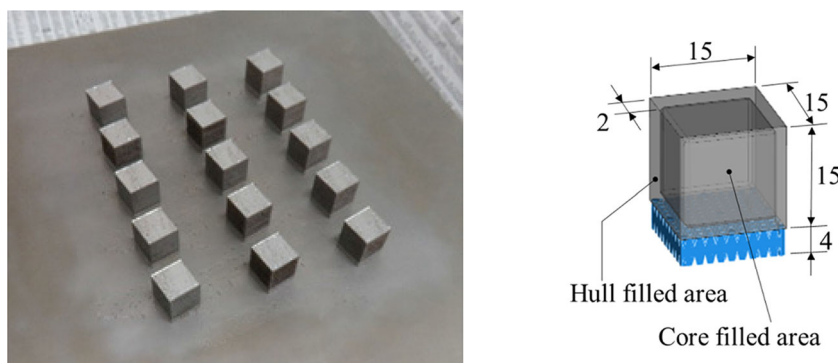
leads to the improvement in porosity of the as-built H13 specimen from 0.07 ± 0.16 to 0.005 ± 0.001 . Thus, HIP is an effective post-process treatment method that can be used, if necessary, to improve the density of the parts.

Figure 6 summarizes these results in the form of a process map of the effects of the laser power and scan speed on the density. For specimens with high densities exceeding 99.7% to be realized, more than 300 W of laser power should be employed, and the scan speed should be lesser than 900 mm/s. Table 4 summarizes the results of previous studies. According to these results, Laakso et al. [16] produced the high-density as-built H13 tool steel having a porosity of less than 0.09% at an energy density of 84.03 J/mm³, comparable with the results of the present study, via the D-optimal design of experiments (DOE) approach. Moreover, Mazur et al. [10] reported a relative density of the as-built specimen of 99.88% at an energy density of 80 J/mm³, which is also similar to the results of the present study. Thus, the high density H13 alloy can be produced via optimization of the fabrication condition.

3.1.2 Influence of process parameters on density of alloy with 1000-W laser

Using the high-power laser of 1000 W should speed up the PBF-LB process. A process map for the 1000-W laser was prepared for comparison with the process map for the 400-W laser. First, the region of the process parameters was narrowed in a preliminary experiment. Then, the process parameters were studied at a laser power range of 600–1000 W, scan speed range of 100–260 mm/s, hatching pitch of 0.7 mm, and layer thickness of 0.1 mm. The energy density range was 34.4–142.9 J/mm³. Figure 7 shows the relation between the energy density and relative density. Figure 7(a) and (b) show the results with varying laser power and scan speed, respectively. The relative density tended to increase with the energy density and became saturated at 99.4% when the energy density was over 80 J/mm³. This trend is similar to that observed for the 400-W laser presented in Fig. 4. The process

Fig. 3 The cubic specimens and the hull-core method



(a) Cubic specimens fabricated using the 1000-W laser (b) Hull-core method

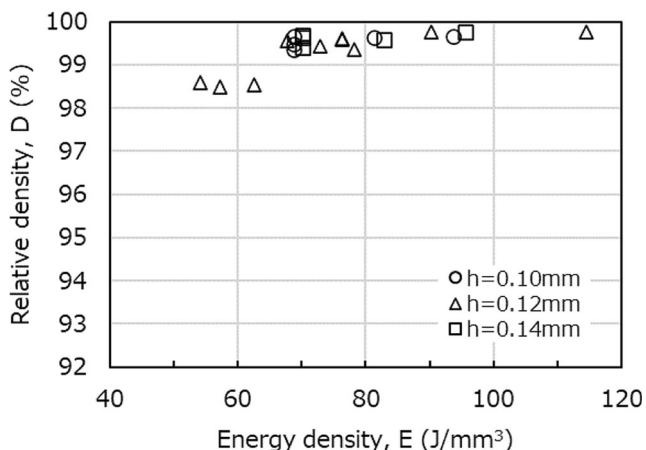
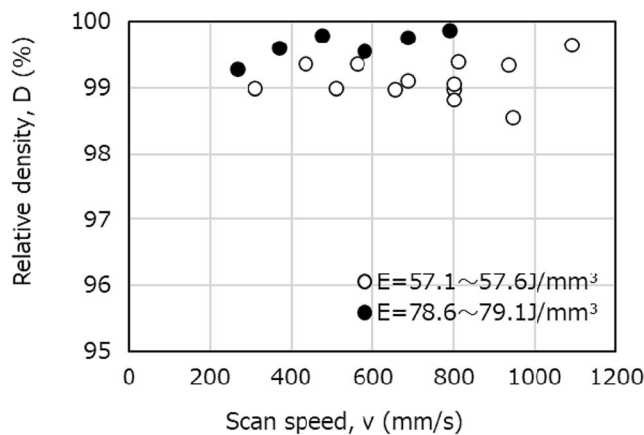


Fig. 4 Relation between the energy density and relative density of the as-built specimens fabricated using the 400-W laser

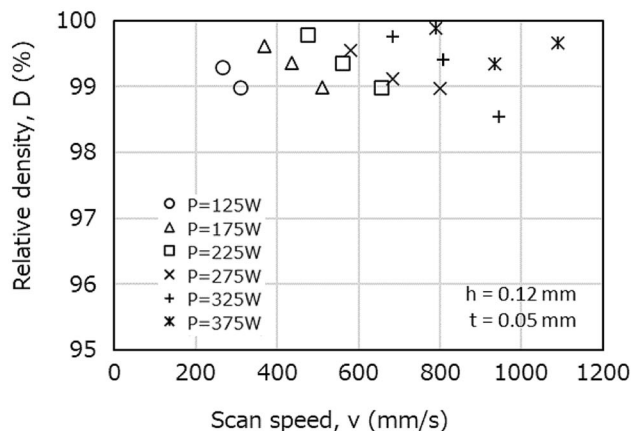
map for the 1000-W laser suggests that it would be difficult to fabricate high-density parts at a scan speed of more than 200 mm/s even at high laser powers of 600–1000 W.

Figure 8 summarizes these results as a process map of the effects of the laser power and scan speed on the density. The maximum relative density of 99.7% was obtained at a laser power of 600 W, scan speed of 100 mm/s, and energy density of 85.7 J/mm³ and is slightly lower than that obtained using the 400-W laser. The fall in density was attributed to melting and solidification phenomena occurring during the laser radiation, such as Marangoni convection in the melt pool, generation of plumes and spatter, and occurrence of keyholes as elucidated by King et al. [27] and other researchers [28–34]. Melting and solidification phenomena occurring when using high-power lasers of more than 500 W have rarely been reported. Our group has previously reported melting and solidification phenomena for Al-10Si-0.4Mg alloy [35], Inconel 718 [36], and pure copper [37] using the same machine. The previous results indicated that a high laser power or high energy density causes large fluctuations in the melt pool because of Marangoni convection and the occurrence of keyholes. These phenomena cause pores and a lack of fusion faults as well as large amounts of spatter. If spatter falls on the powder bed, this can cause a lack of fusion faults owing to pore generation or scratching of the powder bed generated by recoating. Thus, the fall in density in the case of the 1000-W laser was attributed to pore generation and the lack of fusion faults.

In addition, it is known that the process parameters are affected by the geometry of the parts in terms of wall thickness, hole and channel diameters, and overhang. Moreover, the geometry of the parts influences their density and residual stress [11–13]. Although this study focuses on the characteristics of the cubic specimens and the fabrication conditions involved, the real parts exhibit geometrically complicated shapes. Therefore, further considerations regarding the



(a)



(b)

Fig. 5 Influence of the laser power and scan speed on the relative density of the as-built specimens fabricated using the 400-W laser: (a) energy density and (b) laser power

geometry must be made. As reported by other researchers [38–41], the control of laser beam using a closed-loop control is required to assure the quality of real parts because the scanner-based laser AM process presents an inherent variation of the temperature due to the scan effect of laser beam [38,

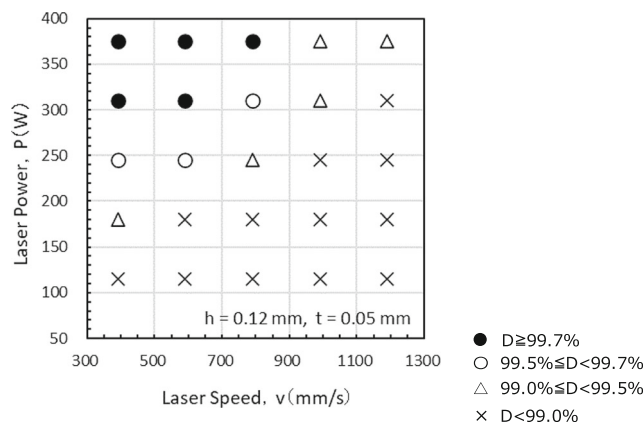


Fig. 6 Process map of the effects of the laser power and scan speed on the relative density of the as-built specimens fabricated using the 400-W laser

Table 4 Results for the relative density and process parameters reported in previous studies and the present study

Process parameters					Relative density or Porosity (%)	References
Laser power (W)	Scan speed (mm/s)	Hatching pitch (mm)	Layer thickness (mm)	Energy density (J/mm ³)		
250.51	993.7	0.09–0.15	0.03	84.03	0.09	Laakso et al. [16]
170	400 or 800				> 99	Mertens et al. [18]
100	300		0.03	111	> 99.5	Krell et al. [19]
280	980	0.12	0.04	59.5	98.6 ± 1	Wang et al. [20]
175	607.64	0.12	0.03	80	99.88	Mazur et al. [10]
100–300	200–1200	0.08 or 0.12	0.04	> 60	Max. 99.7	Narvan et al. [15]
375	790	0.12	0.05	79.1	99.9	The present study

39]. Moreover, the development of the scan strategy algorithms is essential to avoid deformation, deterioration of surface texture, and internal defects of real parts [40, 41].

3.2 Influence of laser power on the microstructure of the as-built specimen

3.2.1 Microstructure of as-built specimen with 400-W laser

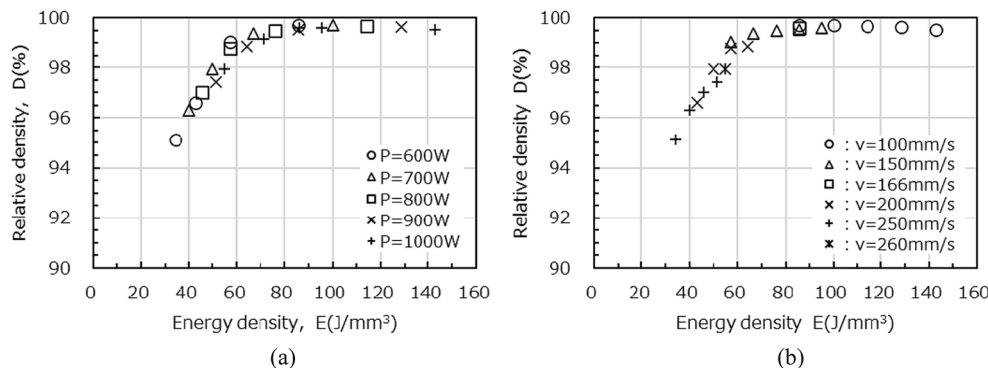
Figure 9 shows the microstructures of the as-built specimens fabricated with energy densities of 57 and 80 J/mm³. Figure 9(a) shows the microstructure of the as-built specimen fabricated at 57 J/mm³ (i.e., a laser power of 375 W, scan speed of 1090 mm/s, hatching pitch of 0.12 mm, and layer thickness of 0.05 mm). Figure 9(b) shows the microstructure of the as-built specimen fabricated at 79.1 J/mm³ (i.e., a laser power of 375 W, scan speed of 790 mm/s, hatching pitch of 0.12 mm, and layer thickness of 0.05 mm). The relative density of the former is 99.7% with a few small pores being observed, as shown in Fig. 9(a), while that of the latter is 99.9% with barely any pores being observed at all, as shown in Fig. 9(b). The melt pool trace of the former had a parabolic shape with a depth of approximately 100 μm and width of 100–200 μm, whereas that of the latter was flat with a depth of

approximately 100 μm and width of over 800 μm. Thus, the melt pool traces had remarkably different aspect ratios, which may have been caused by the difference in energy density from the different scan speeds.

Krell et al. [19] used X-ray diffraction (XRD) and EBSD to show that the microstructure of the as-built H13 tool steel consists of ferrite cells (bcc) with dimensions of 0.1–0.2 μm and austenite walls (fcc) with a thickness of 0.1–0.2 μm. They hypothesized the following model for microstructural evolution: nucleation and growth of δ-Fe (bcc) from the liquid phase, growth of δ-Fe (bcc) and element enrichment of the remaining melt, solidification of the enriched melt as cellular γ-Fe, and the direct transition of δ-Fe to α-Fe (martensite) below the martensite start temperature (*M_s*) as shown by the time-temperature-transformation diagram (TTT-diagram) owing to rapid cooldown of the solid. Narvan et al. [15] reported results similar to those of Krell et al. [19]. They revealed that the microstructure of the as-built specimen consisted of retained austenite with a wall thickness of 100–200 nm and cellular martensite (bcc) with a size of 0.6–1.0 μm.

Figure 10 presents the EBSD results for the (A) vertical and (B) horizontal sections along the build direction. The microstructure of the horizontal section consists of equiaxed grains, while that of the vertical section consists of prolonged grains

Fig. 7 Relation between the energy density and relative density of the as-built specimens fabricated using the 1000-W laser: (a) laser power and (b) scan speed



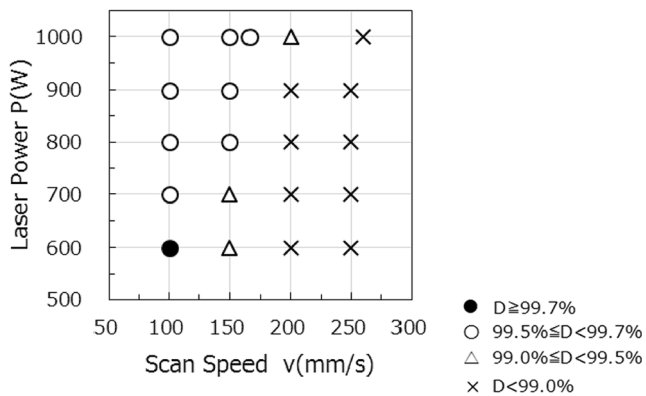
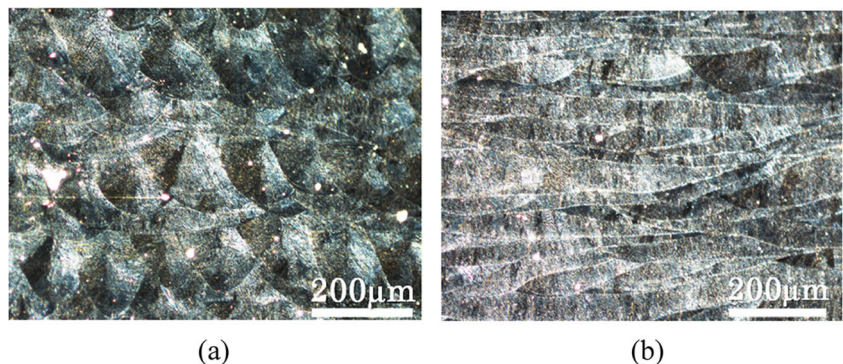


Fig. 8 Process map for the effects of the laser power and scan speed on the relative density of the as-built specimens fabricated using the 1000-W laser in the high-power region

along the build direction. The microstructure of the horizontal section consists of 83.5 vol% martensite (bcc) and 16.5 vol% austenite (fcc) spread within the martensite phase. The microstructure of the vertical section consists of 65.9% bcc and 34.1% fcc; the martensite (bcc) is in the form of columnar grains elongated along the build direction, and the austenite (fcc) is elongated along the boundaries of the martensite grains. Wang et al. [20] obtained phase distribution images of as-built specimens of H13 tool steel fabricated at a laser power of 280 W, scan speed of 980 mm/s, hatching pitch of 0.12 mm, and layer thickness of 0.04 mm, as well as those of as-built specimens heat-treated at 600 °C for 4 h. The ratios of austenite in the as-built and heat-treated specimen were 18% and 5.3%, respectively. Narvan et al. [15] examined the ratio of martensite to austenite in as-built specimens, and Krell et al. [19] found that the ratio of martensite to austenite changes with the cooling rate. Figure 11 shows the grain size distributions of the vertical and horizontal sections of the specimens fabricated using the 400-W laser and obtained with EBSD. Both the vertical and horizontal sections had grain sizes of around 1 μm , but the former had more grains that were more than 2 μm in size than the latter. Other researchers [15, 19, 20] have also reported grain sizes of around 1 μm . Thus, these results are similar to those reported in literature.

Fig. 9 Microstructures of the as-built specimens fabricated using the 400-W laser: (a) $E = 57.3 \text{ J/mm}^3$ and (b) $E = 79.1 \text{ J/mm}^3$



3.2.2 Comparison of microstructures of the as-built specimen with 400-W and 1000-W laser

Using the 1000-W laser, specimens were fabricated via the hull-core method. The microstructure of the as-built specimen fabricated using the 1000-W laser ($E = 85.7 \text{ J/mm}^3$, laser power: 600 W, scan speed: 100 mm/s, hatch pitch: 0.7 mm, layer thickness: 0.1 mm) is shown in Fig. 12. The melt pool trace with a depth of over 200 μm and width of over 800 μm was much larger than that of the 400-W laser at a similar energy density.

Figure 13 presents the EBSD results for the (A) horizontal and (B) vertical sections of the core at a laser power of 600 W, scan speed of 100 mm/s, hatching pitch of 0.7 mm, and layer thickness of 0.1 mm. Although the hull, which was fabricated using the 400-W laser, showed a columnar structure, the core that was fabricated using the 1000-W laser showed an equiaxed structure. The horizontal and vertical sections of the core had grain sizes of approximately 1 μm , similar to the results for the hull. The ratio of martensite to austenite in the horizontal and vertical sections of the core was also similar to that of the hull. Niendorf et al. [42] reported that the hull of a 316L stainless steel specimen fabricated using a 400-W laser showed an equiaxed structure, whereas the core of the specimen fabricated using a 1000-W laser showed a coarse elongated columnar structure along the building direction. The microstructure of the core of the H13 tool steel specimen was significantly different from that of the 316L stainless steel specimen. This is because the H13 tool steel has a cellular structure of $\alpha\text{-Fe}$ surrounded by retained $\gamma\text{-Fe}$ during processing, whereas the 316L stainless steel is strongly affected by heat flow because it only contains austenite during processing. Thus, the microstructure depends on the characteristics of the material.

4 Conclusions

In this study, parameter optimization was performed for the PBF process with H13 tool steel under low- and high-power conditions. The effects of process parameters such as the laser power, scan speed, and hatching pitch on the density and

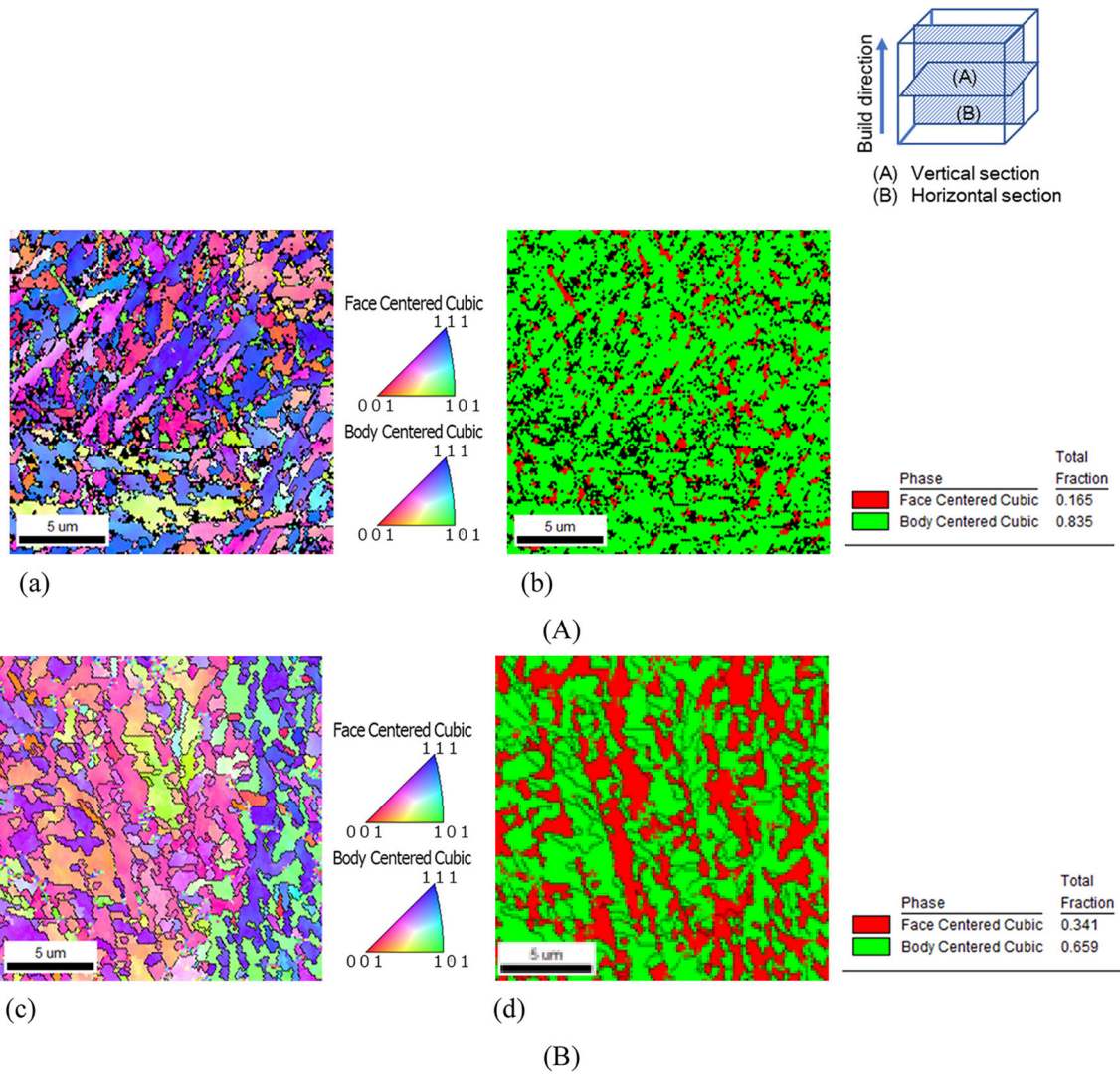


Fig. 10 EBSD grain orientation maps of specimens fabricated using the 400-W laser: (a) IPF map and (b) phase distribution image of the (A) vertical section along the build direction; (c) IPF map and (d) phase distribution image of the (B) horizontal section along the build direction

microstructure of the as-built H13 tool steel were investigated. The following results were obtained.

- Using the 400-W laser, the highest density of 99.9% was obtained at a laser power of 375 W, scan speed of 790

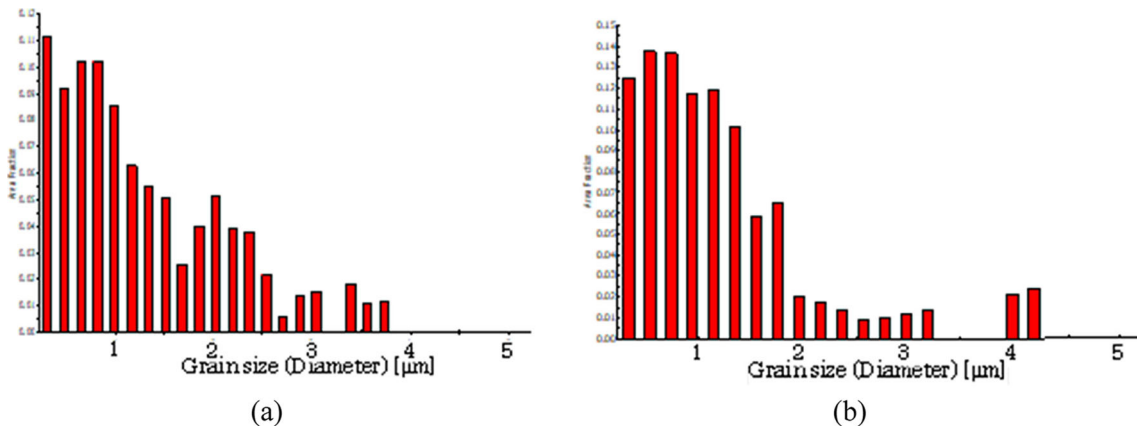


Fig. 11 Grain size distribution of specimens fabricated using the 400-W laser obtained with EBSD: (a) vertical and (b) horizontal sections along the build direction

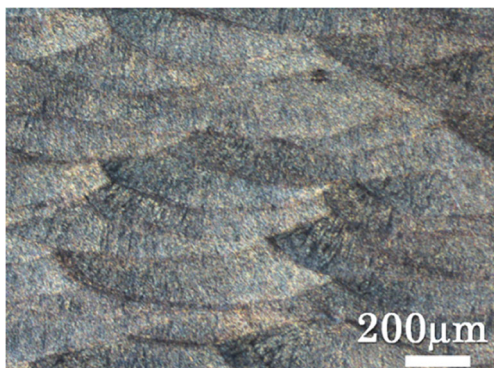


Fig. 12 Microstructure of the as-built specimen fabricated using the 1000-W laser ($E = 85.7 \text{ J/mm}^3$, laser power: 600 W, scan speed: 100 mm/s, hatch pitch: 0.7 mm, layer thickness: 0.1 mm)

mm/s, hatch pitch of 0.12 mm, layer thickness of 0.05 mm, and energy density of 79.1 J/mm^3 .

- Using the 400-W laser, the EBSD analysis showed that as-built specimen fabricated in consideration of the optimum process parameters had a prolonged columnar microstructure in the build direction. In addition, the phase distribution images showed that the specimen consisted of martensite (bcc) and austenite (fcc) with a grain size of around $1 \mu\text{m}$.

- Using the 1000-W laser, the highest density of 99.7% was obtained at a laser power of 600 W, scan speed of 100 mm/s, hatch pitch of 0.7 mm, layer thickness of 0.1 mm, and energy density of 85.7 J/mm^3 . The density was slightly lower than that using the 400-W laser.
- Using the 1000-W laser, the specimens were fabricated via the hull-core method. The EBSD analysis identified that the hull and core of the as-built specimen showed prolonged columnar and equiaxed microstructures, respectively. The phase distribution images showed that the specimen consisted of martensite (bcc) and austenite (fcc) with a grain size of around $1 \mu\text{m}$.

Thus, it was found that the specimen density using the 400-W laser is slightly higher than that using the 1000-W laser, and the microstructure of the as-built specimen using the 400-W laser is different from that using the 1000-W laser.

In addition, with regard to the possibility of speeding up the process using the high-power laser, as an example, considering a part of $10 \text{ mm} \times 10 \text{ mm} \times 0.1 \text{ mm}$ with the maximum density parameters of the 400-W laser (laser power: 375 W, scan speed: 790 mm/s, hatch pitch: 0.12 mm, layer thickness: 0.05 mm) and the 1000-W laser (laser power: 600 W, scan speed: 100 mm/s, hatch pitch: 0.7 mm, layer thickness: 0.1

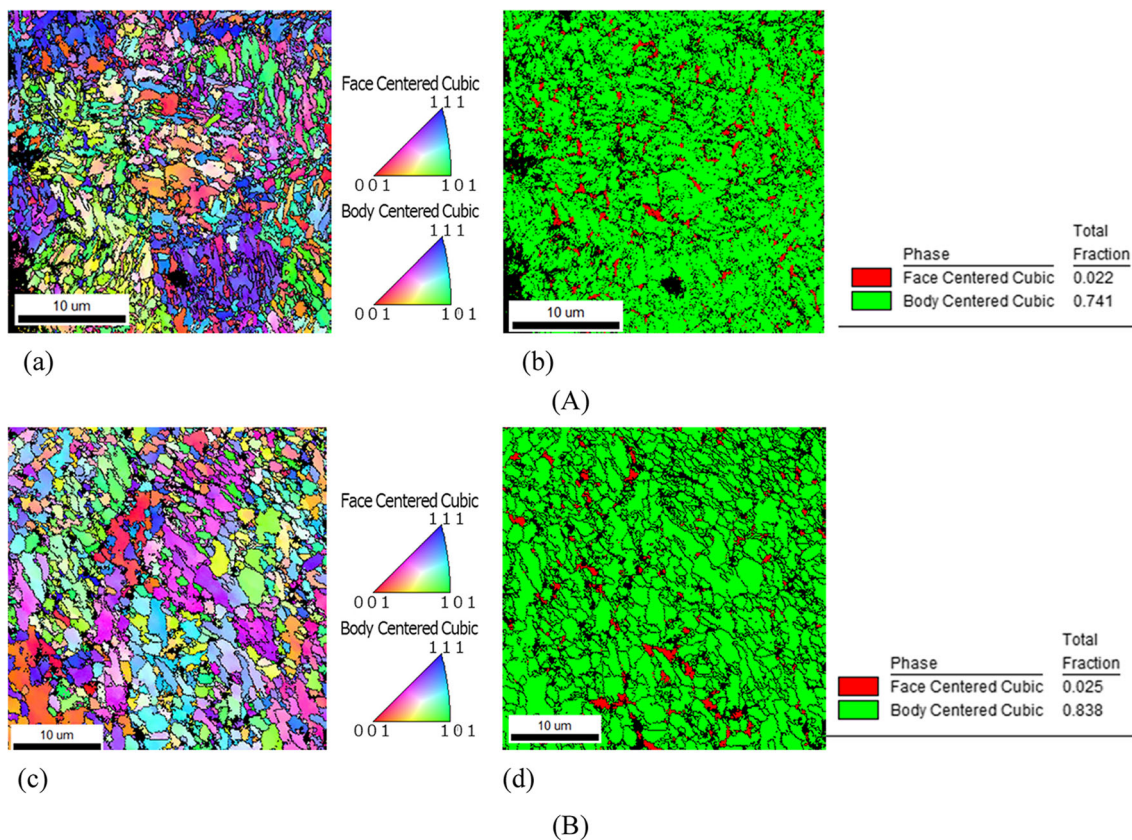


Fig. 13 EBSD grain orientation maps of the core part of the specimen fabricated using the 1000-W laser: (a) IPF map and (b) phase distribution image of the (A) vertical section along the build direction; (c) IPF map and (d) phase distribution image of the (B) horizontal section along the build direction

mm) just for core region, one can see that the high-power laser still offers an approximate 30% processing time reduction for H13 steel. Because its scan speed is nearly 8-fold lower, but its hatch pitch is 7-fold and its layer thickness is 2-fold higher. Thus, it was found that the processing time can be reduced by approximately 30%.

References

- Bourell D, Kruth JP, Leu M, Levy G, Rosen D, Beese AM, Clare A (2017) Materials for additive manufacturing. *CIRP Ann Manuf Technol* 66:659–681
- Debroy T, Wei HL et al (2018) Additive manufacturing of metallic components – process, structure and properties. *Prog Mater Sci* 92: 112–224
- Niu HJ, Chang ITH (1998) Liquid phase sintering of M3/2 high speed steel by selective laser sintering. *Scr Mater* 39:67–72
- Niu HJ, Chang ITH (1999) Selective laser sintering of gas and water atomized high speed steel powders. *Scr Mater* 41:25–30
- Asgharzadeh H, Simchi A (2005) Effect of sintering atmosphere and carbon content on the densification and microstructure of laser-sintered M2 high-speed steel powder. *Mater Sci Eng A* 403:290–298
- Xie JW, Fox P, O’Neill W, Sutcliffe CJ (2005) Effect of direct laser re-melting processing parameters and scanning strategies on the densification of tool steels. *J Mater Process Technol* 170:516–523
- Kempen K, Vrancken B et al (2014) Selective laser melting of crack-free high density M2 high speed steel parts by baseplate preheating. *J Manuf Sci Eng* 136:061026
- Zhang M, Chen C et al (2018) Laser additive manufacturing of M2 high-speed steel. *Mater Sci Technol* 34:69–78
- Mazur M, Leary M et al (2016) SLM additive manufacture of H13 tool steel with conformal cooling and structural lattices. *Rapid Prototyp J* 22(3):504–518
- Mazur M, Brincat P, Leary M, Brandt M (2017) Numerical and experimental evaluation of a conformally cooled H13 steel injection mould manufactured with selective laser melting. *Int J Adv Manuf Technol* 93:881–900
- Yakout M, Cadamuro A, Elbestawi MA, Veldhuis SC (2017) The selection of process parameters in additive manufacturing for aerospace alloys. *Int J Adv Manuf Technol* 92:2081–2098
- Fayazfar H, Salarian M, Rogalsky A, Sarker D, Russo P, Paserin V, Toyserkani E (2018) A critical review of powder-based additive manufacturing of ferrous alloys: process parameters, microstructure and mechanical properties. *Mater Des* 144:98–128
- Malý M, Höller C, Skalon M, Meier B, Koutný D, Pichler R, Sommitsch C, Paloušek D (2019) Effect of process parameters and high-temperature preheating on residual stress and relative density of Ti6Al4V processed by selective laser melting. *Materials* 12: 930. <https://doi.org/10.3390/ma12060930>
- Vock S, Klöden B, Kirchner A, Weißgärber T, Kieback B (2019) Powders for powder bed fusion: a review. *Prog Addit Manuf* 4: 383–397
- Narvan M, Al-Rubaie KS, Elbestawi M (2019) Process-structure-property relationships of AISI H13 tool steel processed with selective laser melting. *Materials* 12:2284. <https://doi.org/10.3390/ma12142284>
- Laakso P, Riipinen T et al (2016) Optimization and simulation of SLM process for high density H13 tool steel parts. *Phys Procedia* 83:26–35
- Holzweissig MJ, Taube A, Brenne F, Schaper M, Niedorf T (2015) Microstructural characterization and mechanical performance of hot work tool steel processed by selective laser melting. *Metall Mater Trans B* 46B:545–549
- Mertens R, Vrancken B et al (2016) Influence of powder bed preheating on microstructure and mechanical properties of H13 tool steel SLM parts. *Phys Procedia* 83:882–890
- Krell J, Röttger A, Geenen K, Theisen W (2018) General investigations on processing tool steel X40CrMoV5-1 with selective laser melting. *J Mater Process Technol* 255:679–688
- Wang M, Li W et al (2019) High-temperature properties and microstructural stability of the AISI H13 hot-work tool steel processed by selective laser melting. *Metall Mater Trans B* 50B:531–542
- Yan JJ, Zheng DL et al (2017) Selective laser melting of H13: microstructure and residual stress. *J Mater Sci* 52:12476–12485
- Casati R, Coduri M et al (2018) Microstructure and mechanical behavior of hot-work tool steels processed by selective laser melting. *Mater Charact* 137:50–57
- Prudente WR, Fabricio CLJ et al (2017) Microstructural evolution under tempering heat treatment in AISI H13 hot-work tool steel. *Int J Eng Res Appl* 7:67–71
- Sander J, Hufenbach J et al (2016) Microstructure and properties of FeCrMoVC tool steel produced by selective laser melting. *Mater Des* 89:335–341
- Boes J, Röttger A, Mutke C, Escher C, Theisen W (2018) Microstructure and mechanical properties of X65MoCrWV3-2 cold-work tool steel produced by selective laser melting. *Addit Manuf* 23:170–180
- Åsberg M, Fredriksson G, Hatami S, Fredriksson W, Krakhmalev P (2019) Influence of post treatment on microstructure, porosity and mechanical properties of additive manufactured H13 tool steel. *Mater Sci Eng A* 742:584–589
- King WE, Barth HD et al (2014) Observation of keyhole-mode laser melting in laser powder-bed fusion additive manufacturing. *J Mater Process Technol* 214:2915–2925
- King WE, Anderson T et al (2015) Overview of modelling and simulation of metal powder bed fusion process at Lawrence Livermore National Laboratory. *Mater Sci Technol* 31:957–968
- Qiu C, Panwisawas C, Ward M, Basoalto HC, Brooks JW (2015) On the role of melt flow into the surface structure and porosity development during selective laser melting. *Acta Mater* 96:72–79
- Khairallah SA, Anderson AT, Rubenchik AM, King WE (2016) Laser powder-bed fusion additive manufacturing: physics of complex melt flow and formation mechanisms of pores, spatter, and denudation zones. *Acta Mater* 108:36–45
- Matthews MJ, Guss G et al (2016) Denudation of metal powder layers in laser powder bed fusion processes. *Acta Mater* 114:33–42
- Martin AA, Calta NP et al (2019) Dynamics of pore formation during laser powder bed fusion additive manufacturing. *Nat Commun* 10:1987. <https://doi.org/10.1038/s41467-019-10009-2>
- Cunningham R, Zhao C et al (2019) Keyhole threshold and morphology in laser melting revealed by ultrahigh-speed x-ray imaging. *Science* 363:849–852
- Kyogoku H, Ikeshoji T-T (2020) A review of metal additive manufacturing technologies: mechanism of defects formation and simulation of melting and solidification phenomena in laser powder bed fusion process. *Mech Eng Rev* 7(1):19–00182
- Araki M, Kusaka S et al (2018) Parameter optimization on the fabrication of Al-10Si-0.4Mg alloy using selective laser melting process. *J Jpn Soc Powder Powder Metallurgy* 65:383–388
- Tachibana Y, Ikeshoji T-T, Nakamura K, Yonehara M, Kyogoku H (2018) Selective laser melting of Inconel 718 under high power and high scanning speed conditions. *Mater Sci Forum* 941:1574–1577
- Ikeshoji T-T, Nakamura K, Yonehara M, Imai K, Kyogoku H (2018) Selective laser melting of pure copper. *JOM* 70:396–400

38. Calleja A, Tabernero I et al (2014) Feed rate calculation algorithm for the homogeneous material deposition of blisk blades by 5-axis laser cladding. *Int J Adv Manuf Technol* 74:1219–1228
39. Yeung H, Lane B, Fox J (2019) Part geometry and conduction-based laser power control for powder bed fusion additive manufacturing. *Addit Manuf* 30:100844
40. Martínez S, Lamikiz A et al (2017) Analysis of the regimes in the scanner-based laser hardening process. *Opt Lasers Eng* 90:72–80
41. Valente EH, Gundlach C et al (2019) Effect of scanning strategy during selective laser melting on surface topography, porosity, and microstructure of additively manufactured Ti-6Al-4V. *Appl Sci* 9:5554. <https://doi.org/10.3390/app9245554>
42. Niendorf T, Leuders S et al (2013) Highly anisotropic steel processed by selective laser melting. *Metall Mater Trans B* 44B:749–796

Publisher's note Springer Nature remains neutral with regard to jurisdictional claims in published maps and institutional affiliations.